

High-Throughput Computational Study and Machine Learning Prediction of Electronic Properties in Transition Metal Dichalcogenide/Two-Dimensional Layered Halide Perovskite Heterostructures

Congsheng Xu, Xiaomei Deng, and Peiyuan Yu*



Cite This: *ACS Appl. Mater. Interfaces* 2024, 16, 55970–55980



Read Online

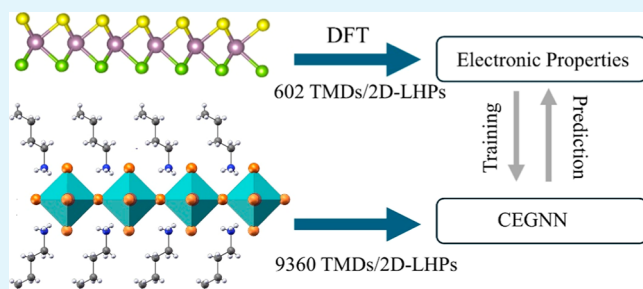
ACCESS |

Metrics & More

Article Recommendations

Supporting Information

ABSTRACT: Heterostructures formed by transition metal dichalcogenides (TMDs) and two-dimensional layered halide perovskites (2D-LHPs) have attracted significant attention due to their unique optoelectronic properties. However, theoretical studies face challenges due to the large number of atoms and the need for lattice matching. With the discovery of more 2D-LHPs, there is an urgent need for methods to rapidly predict and screen TMDs/2D-LHPs heterostructures. This study employs first-principles calculations to perform high-throughput computations on 602 TMDs/2D-LHPs heterostructures. Results show that different combinations exhibit diverse band alignments, with MoS₂ and WS₂ more likely to form type-II heterostructures with 2D-LHPs. The highest photoelectric conversion efficiency of type-II structures reaches 23.26%, demonstrating potential applications in solar cells. Notably, some MoS₂/2D-LHPs form type-S structures, showing promise in photocatalysis. Furthermore, we found that TMDs can significantly affect the conformation of organic molecules in 2D-LHPs, thus modulating the electronic properties of the heterostructures. To overcome computational cost limitations, we constructed a crystal graph convolutional neural network model based on the calculated data to predict the electronic properties of TMDs/2D-LHPs heterostructures. Using this model, we predicted the bandgaps and band alignment types of 9,360 TMDs/2D-LHPs heterostructures, providing a comprehensive theoretical reference for research in this field.



KEYWORDS: *transition metal dichalcogenides, two-dimensional layered halide perovskites, heterostructure, band alignment, equivariant graph neural network*

INTRODUCTION

In recent years, two-dimensional (2D) materials have garnered extensive attention from researchers due to their unique optoelectronic properties and broad application prospects.^{1–3} Among the numerous 2D materials, transition metal dichalcogenides (TMDs) and 2D-LHPs stand out with their promising carrier transport properties, rich spectral absorption characteristics, and tunable band structures.^{4,5} TMDs, with their atomic thickness, large specific surface area, and good mechanical flexibility, demonstrate enormous application potential in fields such as photodetection, photocatalysis, and photovoltaic devices.^{6–8} Concurrently, 2D-LHPs materials are highly favored for their structural diversity, low cost, and exceptional defect tolerance, exhibiting attractive application prospects in optoelectronic devices.^{9,10} Recent studies have shown that forming heterostructures by combining TMDs with 2D-LHPs can generate novel optoelectronic properties based on the respective advantages of both materials, potentially overcoming the performance bottlenecks of current optoelectronic devices.^{11–14} For instance, Karpińska et al. confirmed

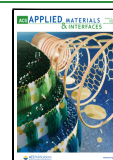
the existence of hole transfer and energy transfer in the WS₂/2D-LHPs heterostructure through steady-state reflectance and photoluminescence (PL) studies.¹⁵ Wang et al. have demonstrated that 2D-LHPs, as excellent light-absorbing components, can significantly enhance the overall performance of photodetectors based on 2D TMDs. Significantly enhanced PL has been observed in the WS₂ and quasi-2D perovskite heterostructure.¹⁶ Xie et al. realized room-temperature visible-infrared broadband non-volatile optoelectronic memory based on few-layer MoS₂/2D-LHPs van der Waals (vdW) heterostructure, providing a new route for fast, low-power, and multibit optoelectronic memory from visible to infrared wavelengths.¹⁷

Received: July 18, 2024

Revised: September 22, 2024

Accepted: September 23, 2024

Published: October 3, 2024



However, to achieve efficient optoelectronic conversion in TMDs/2D-LHPs heterostructures, precise control of the interfacial band alignment is crucial. Based on the relative positions of the band alignment, TMDs/2D-LHPs heterostructures can be classified into three types: type-I, type-II, and type-III.¹³ Different types of band alignments have significant impacts on the separation and recombination dynamics of photogenerated carriers, thereby affecting the optoelectronic conversion efficiency of the heterostructures. For example, type-II band alignment facilitates the spatial separation of photogenerated electrons and holes, while type-I band alignment is more prone to carrier recombination.^{18–21} Furthermore, an S-type band alignment has been discovered in TMDs/2D-LHPs heterostructures. This S-type alignment facilitates efficient charge transfer, improves the separation of photogenerated electrons and holes, and thereby enhances their photocatalytic potential.^{14,22} Therefore, a deep understanding and regulation of the band alignment in TMDs/2D-LHPs heterostructures are essential for optimizing their optoelectronic performance. Currently, research on the band structure of TMDs/2D-LHPs heterostructures is mainly limited to a few common material combinations, such as MoS₂/BA₂PbI₄, WS₂/BA₂PbI₄ and WS₂/(PEA)₂PbI₄.^{14,15,22} Although these studies have revealed the band alignment characteristics of certain heterostructures, it remains challenging to establish universal structure–property relationships. With the discovery of more 2D perovskite materials, there is an urgent need to systematically explore the band structure rules and influencing factors of TMDs and 2D-LHPs heterostructures on a broader scale. This not only helps deepen the understanding of the charge transfer mechanisms at heterostructure interfaces but also provides theoretical guidance for the rational design of high-performance optoelectronic devices in the future.

High-throughput screening based on first-principles calculations provides a powerful tool for large-scale exploration of the electronic properties of heterostructures.^{23–25} Through high-throughput computations, structural and property data of a large number of material combinations can be rapidly obtained, accelerating the process of discovering novel high-performance heterostructures.^{26–28} Additionally, by combining the massive data generated from high-throughput calculations with machine learning methods, the efficiency and accuracy of material screening can be further enhanced. In recent years, material representation and property prediction methods based on Graph Neural Networks (GNN) have garnered increasing attention from researchers. GNNs can automatically learn the structural features of materials, establishing high-dimensional nonlinear mapping relationships between structure and properties, enabling rapid property prediction of materials.^{29–32} However, directly applying GNN to the study of 2D TMDs/2D-LHPs heterostructures still faces several challenges. On one hand, traditional GNN models mainly handle fixed-size molecular graphs, making them difficult to apply to 2D heterostructure structures with an indefinite number of atoms.^{33,34} On the other hand, the properties of 2D materials must remain invariant to transformations such as lattice translation and rotation, and must satisfy periodic boundary conditions.^{35–37}

In this work, we designed a series of TMDs/2D-LHPs heterostructures from scratch and systematically investigated their band structure characteristics and influencing factors using first-principles calculations. The study revealed that

heterostructures formed by different TMDs and 2D perovskites exhibit various types of band alignment, which is closely related to the bandgap size of the TMDs. Some TMDs, such as MoS₂, can form ideal type-II heterostructures with specific perovskites, which is beneficial for charge separation in photocatalytic reactions. Furthermore, through molecular dynamics simulations, we discovered that TMDs have a significant impact on the conformations of organic molecules in the perovskite layer, thereby influencing its electronic properties, providing a new approach for modulating the electronic properties of heterostructures. Based on the extensive data obtained on the band structures of heterostructures, we further proposed a crystal equivariant graph neural network (CEGNN) model that enables rapid prediction of the electronic properties of TMDs/2D-LHPs heterostructures and predicted the electronic properties and band alignment of currently available 2D-LHPs and TMDs heterostructures. This study deepens the understanding of the band modulation mechanism in TMDs/2D-LHPs heterostructures, and the constructed CEGNN model provides a powerful tool for high-throughput screening of novel high-performance TMDs/2D-LHPs optoelectronic materials, which has important guiding significance for the rational design of related devices.

■ COMPUTATIONAL METHOD

The results of the first-principles calculations were performed using the Vienna Ab Initio Simulation Package, employing the Perdew–Burke–Ernzerhof (PBE) functional within the generalized gradient approximation to describe the exchange–correlation functional.^{38,39} The crystal structures were fully relaxed, with convergence criteria for energy and forces set to below 10^{−6} eV and 10^{−2} eV/Å per atom, respectively. A cutoff energy of 400 eV was used, and vdW interactions were corrected using the DFT-D3 method.⁴⁰ To ensure the accuracy of the calculations, extensive convergence analyses were carried out. Structural optimization and electronic properties calculations utilized a Γ-centered Monkhorst–Pack *k*-point grid of 2 × 2 × 1 and 3 × 3 × 1, respectively. To prevent interactions between periodically repeated slabs, a large vacuum space of approximately 20 Å was used in the *z*-direction.

Molecular dynamics simulations were performed using the CP2K package.⁴¹ An NVT ensemble was employed, with simulation temperatures of 300 K, a time step of 1 fs, and a total simulation time of 10,000 steps, corresponding to 10 ps. Temperature control was maintained using a Nose–Hoover thermostat with a coupling time of 50 fs. The exchange–correlation functional was the PBE functional, with vdW interactions also corrected using the DFT-D3 method.⁴⁰ The interaction potentials between atoms were described by the Goedecker–Teter–Hutter (GTH) pseudopotentials, and the plane wave basis set used was DZVP-MOLOPT-SR-GTH.⁴² Periodic boundary conditions were applied in the XY directions for the simulation box.

The estimated photoelectric conversion efficiency (PCE) is obtained using Scharber's method,⁴³ in which the upper limit of the PCE in the limit of 100% external quantum efficiency can be expressed as following

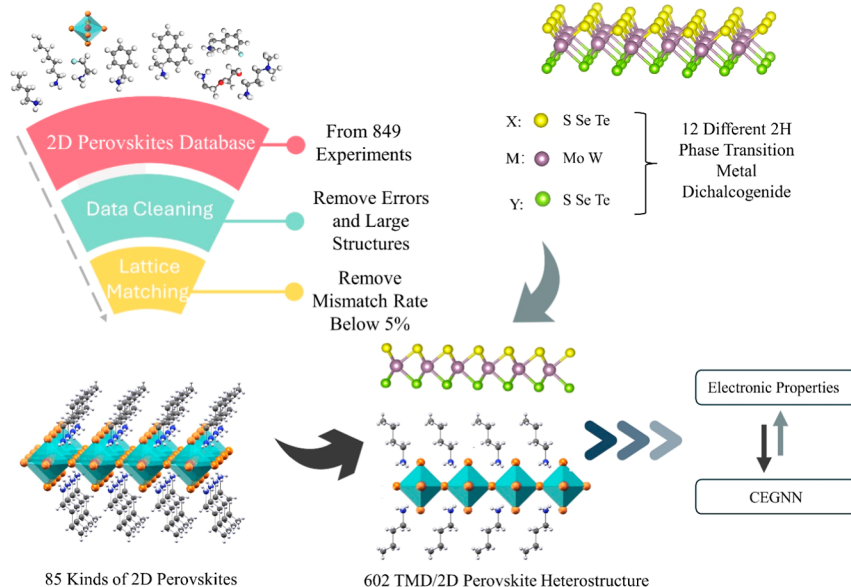


Figure 1. Data screening process. From 849 experiments, 85 qualified 2D-LHP structures were selected.⁴⁴ The TMDs include MoS₂, MoSe₂, MoTe₂, WS₂, WSe₂, WTe₂, and Janus structures such as MoSSe, MoSTe, MoSeTe, WSSe, WSTe, and WSeTe. In total, 602 TMDs/2D-LHPs were studied.

$$\eta = \frac{J_{sc} V_{oc} \beta_{FF}}{P_{solar}} = \frac{0.65(E_g^d - \Delta E_c - 0.3) \int_{E_g}^{\infty} \frac{P(\hbar\omega)}{\hbar\omega} d(\hbar\omega)}{\int_0^{\infty} P(\hbar\omega) d(\hbar\omega)} \quad (1)$$

where β_{FF} is the band fill factor, which is commonly approximated as 0.65. This value is a simplification based on empirical observations; while it provides a useful estimate, the actual value may vary depending on the specific characteristics of the solar cell. The maximum open circuit voltage V_{oc} is estimated using $E_g^d - \Delta E_c - 0.3$, where E_g^d is the band gap of the donor and ΔE_c is the conduction band offset. $P(\hbar\omega)$ is the AM1.5 solar energy flux at the photon energy $\hbar\omega$. AM1.5 stands for “Air Mass 1.5”, which is a standard solar spectrum used to simulate the solar energy received at the Earth’s surface. It represents the solar radiation that reaches the surface after passing through a thickness of 1.5 times the Earth’s atmosphere, typically corresponding to an angle of approximately 48 degrees from the zenith.

To construct the CEGNN, we utilize EGNNS, which can satisfy rotation and translation invariance properties.³⁵ We do not specify chemical bonds between atoms; instead, we treat the crystal structure as a point cloud, represented as a fully connected graph $G = (V, E)$, where V is the set of nodes representing all atoms in the crystal, and E is the set of edges encompassing all connections between nodes, simulating the interactions between all atoms $v_i \in V$. Each node v_i is embedded with coordinates $x_i \in \mathbb{R}^3$ and atomic features $h_i \in \mathbb{R}^d$. EGNNS consist of L equivariant graph neural layers, each layer defined as follows

$$\mathbf{m}_{ij} = \phi_e(\mathbf{h}_i^l, \mathbf{h}_j^l, d_{ij}^2, e_{ij}) \quad (2)$$

$$\mathbf{h}_i^{l+1} = \phi_h(\mathbf{h}_i^l, \sum_{j \neq i} \mathbf{m}_{ij}; \theta_h) \quad (3)$$

$$\mathbf{x}_i^{l+1} = \mathbf{x}_i^l + \sum_{j \neq i} \frac{\mathbf{x}_i^l - \mathbf{x}_j^l}{d_{ij} + 1} \phi_x(\mathbf{h}_i^l, \mathbf{h}_j^l, d_{ij}^2, e_{ij}) \quad (4)$$

where, $d_{ij} = \|\mathbf{x}_i^l - \mathbf{x}_j^l\|_2$ represents the pairwise Euclidean distance between atoms v_i and v_j in the l -th layer. All learnable functions, namely ϕ_e, ϕ_h and ϕ_x , are parametrized by multilayer perceptrons (MLPs).

In crystal structures, atomic coordinates are typically represented using fractional coordinates, which are relative to the unit cell basis vectors. Additionally, crystals exhibit periodicity, meaning atoms can interact with atoms in other unit cells across the unit cell boundaries. To correctly handle these characteristics in CEGNN, we need to account for the periodicity when calculating interatomic distances.

The specific steps are as follows: first, convert the fractional coordinates of the two arbitrary atoms to Cartesian coordinates. We denote the fractional coordinates of the two atoms as (u_1, v_1, w_1) and (u_2, v_2, w_2) :

For atom 1

$$\begin{pmatrix} x_1 \\ y_1 \\ z_1 \end{pmatrix} = u_1 \mathbf{a} + v_1 \mathbf{b} + w_1 \mathbf{c} \quad (5)$$

For atom 2

$$\begin{pmatrix} x_2 \\ y_2 \\ z_2 \end{pmatrix} = u_2 \mathbf{a} + v_2 \mathbf{b} + w_2 \mathbf{c} \quad (6)$$

The radial distance d_{ij} between the two atoms in Cartesian coordinates is the Euclidean distance:

$$d_{ij} = \sqrt{(x_2 - x_1)^2 + (y_2 - y_1)^2 + (z_2 - z_1)^2} \quad (7)$$

For each Cartesian coordinate difference, adjust for periodicity

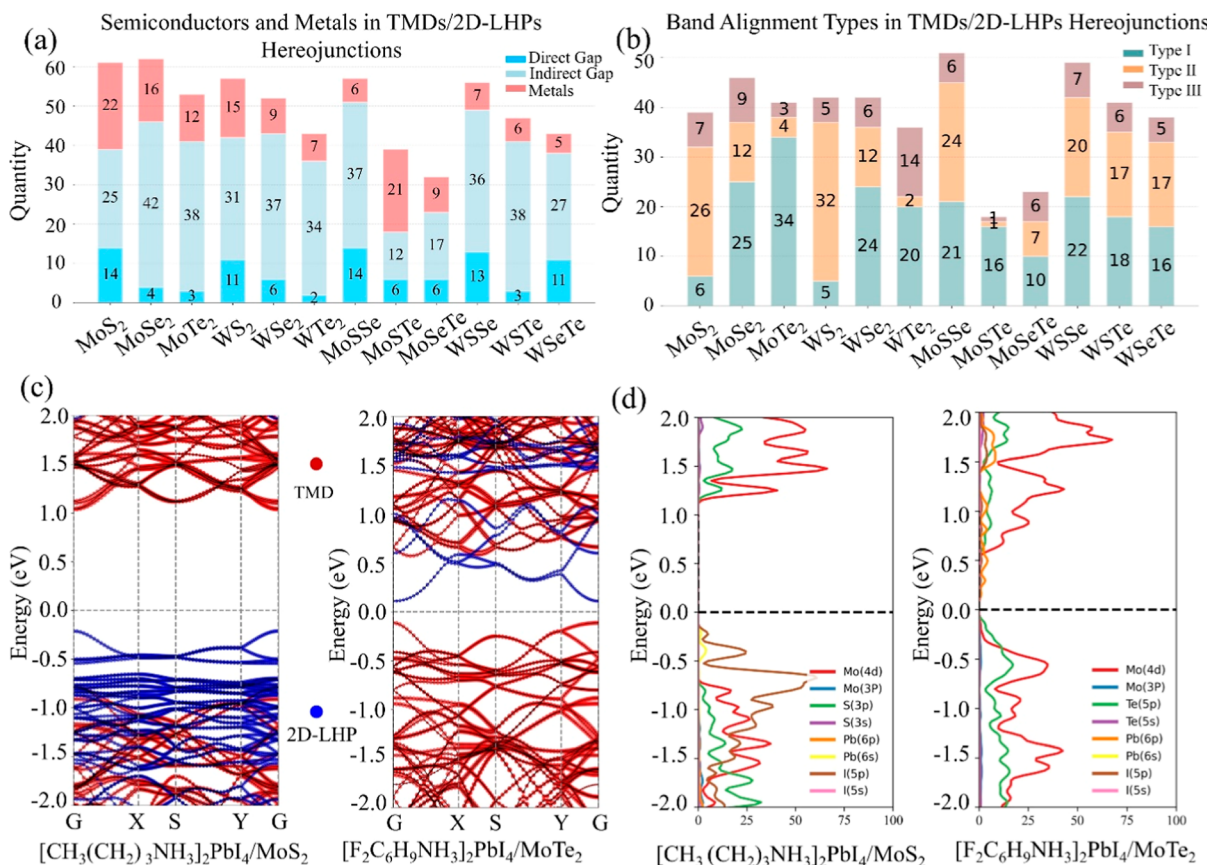


Figure 2. (a) Statistics of the electronic properties of heterostructures formed between various TMDs and 2D-LHPs, including metallic and semiconductor properties, as well as direct and indirect bandgaps among the semiconductor properties. (b) Statistics of the band alignment types of TMDs/2D-LHPs heterostructures. (c) and (d): projected density of states (PDOS) of $[CH_3(CH_2)_3NH_3]_2PbI_4/MoS_2$ and $[F_2C_6H_9NH_3]_2PbI_4/MoTe_2$, respectively.

$$\Delta x = x_2 - x_1 - a \cdot \text{round}\left(\frac{x_2 - x_1}{a}\right) \quad (8)$$

$$\Delta y = y_2 - y_1 - b \cdot \text{round}\left(\frac{y_2 - y_1}{b}\right)$$

$$\Delta z = z_2 - z_1 - c \cdot \text{round}\left(\frac{z_2 - z_1}{c}\right) \quad (9)$$

Recompute the Radial Distance with Periodic Adjustments

$$d_{ij} = \sqrt{\Delta x^2 + \Delta y^2 + \Delta z^2} \quad (10)$$

■ RESULT AND DISCUSSION

To construct heterostructures of TMDs and 2D-LHPs, we first screened the 2D-LHPs. Figure 1 shows our screening process. We obtained 849 experimentally acquired 2D-LHPs structures from the 2D-LHPs database as the initial data set.⁴⁴ During the preliminary screening, we excluded structures with obvious errors, such as unreasonable structures or duplicate atoms. To balance computational cost and accuracy, we limited the molecular size and excluded perovskite samples with large molecular structures to ensure the feasibility and efficiency of subsequent calculations. In selecting TMDs materials, we considered 12 different 2H phase two-dimensional materials, including MoS₂, MoSe₂, MoTe₂, WS₂, WSe₂, WTe₂, and Janus structures MoSSe, MoSTe, MoSeTe, WSSe, WSTe, and WSeTe. These materials have been partially used in recent

studies to form heterostructures with 2D-LHPs and have shown excellent optoelectronic properties.^{22,43} Based on these successful cases, we further expanded the research scope to explore more combinations of TMDs and 2D-LHPs. When constructing heterostructure structures of 2D-LHPs and TMDs, considering that 2D-LHPs are sensitive to strain, we controlled the lattice mismatch rate to below 5% through supercell operations to ensure the stability of the heterostructures and to obtain a sufficient amount of data. Additionally, to avoid excessive computational load, we excluded heterostructures with more than 600 atoms after the supercell expansion. After these screening and optimization steps, we finally identified 85 types of 2D-LHPs and constructed 602 TMDs/2D-LHPs heterostructures. After obtaining the screened heterostructure structures, we optimized the geometric structure of the heterostructures and calculated their electronic properties and band structures using density functional theory (DFT) calculations.

In Figure 2a, we have analyzed the electronic properties of heterostructures formed between different types of TMDs and various 2D-LHPs, including metallic and semiconductor properties, as well as direct and indirect bandgaps among the semiconductor properties. The results indicate that among the 12 studied TMDs, the number of heterostructures exhibiting semiconductor properties exceeds those exhibiting metallic properties. This suggests that the electronic structures of TMDs and 2D-LHPs are relatively compatible, making them more likely to form semiconductor heterostructures. It is

noteworthy that our bandgap calculation results are based on PBE pseudopotentials, a method that typically underestimates the bandgap size. Therefore, the actual number of heterostructures exhibiting semiconductor properties may be higher than currently reported.

When analyzing heterostructures formed by MoS₂, WS₂, MoSe₂, and WS₂ with 2D-LHPs, we found that the proportion of direct bandgaps in these combinations is higher than in others, which may be due to the more favorable band alignment in these combinations for forming direct bandgaps. To further investigate this, we have categorized the band alignment types of TMDs/2D-LHPs heterostructures in Figure 2b into three types: type-I, type-II, and type-III. Type-I band alignment refers to the conduction band minimum (CBM) and the valence band maximum (VBM) being concentrated in the same material. Type-II band alignment indicates that the CBM is located in one material, while the VBM is in another material. Type-III band alignment, also known as staggered band alignment, refers to the arrangement at the interface of two materials where the CBM of one material is lower in energy than the VBM of the other material.

Our study found that most heterostructures formed between monolayer MoS₂ or WS₂ and 2D-LHPs exhibit type-II band alignment. To gain a deeper understanding of the origin of this band alignment, we analyzed the band structures of the heterostructures formed by the TMDs and 2D-LHPs. The results indicate that in type-II band alignment, the electronic states of the conduction band (CB) are mainly contributed by the TMDs, while the electronic states of the valence band (VB) are primarily contributed by the 2D-LHPs. To visually demonstrate the characteristics of the band alignment, we randomly selected a representative heterostructure of butylammonium lead iodide ($[\text{CH}_3(\text{CH}_2)_3\text{NH}_3]^2\text{PbI}_4/\text{MoS}_2$).⁴⁵ Figure 2c shows the projected band structure of this heterostructure. It can be seen from the figure that the CBM of the heterostructure is mainly contributed by MoS₂, while the VBM is primarily from $[\text{CH}_3(\text{CH}_2)_3\text{NH}_3]^2\text{PbI}_4$, presenting a typical type-II band alignment. To gain a deeper understanding of the properties of electrons, we calculated the PDOS and analyzed the decomposed charge density at the CBM and VBM. The results of the PDOS are shown in Figure 2d, while the details of the decomposed charge density can be found in Figure S1. Through the analysis of PDOS and charge density, we found that in the $[\text{CH}_3(\text{CH}_2)_3\text{NH}_3]^2\text{PbI}_4/\text{MoS}_2$ heterostructure, the electronic states at the CBM primarily originate from the 4d orbitals of Mo atoms and the 3p orbitals of S atoms in the MoS₂ layer, which is consistent with the inherent band structure characteristics of MoS₂. In contrast, the electronic states at the VBM mainly come from the 6s orbitals of Pb atoms and the 5p orbitals of I atoms in the inorganic layer PbI₄ of $[\text{CH}_3(\text{CH}_2)_3\text{NH}_3]^2\text{PbI}_4$.

For other TMDs forming type-II band alignment heterostructures with 2D-LHPs, we observed different situations compared to the MoS₂ and WS₂ systems. For instance, in heterostructures formed by MoTe₂ and WTe₂ with 2D-LHPs, the electronic states of the CB are mainly contributed by the 2D-LHPs, while the VB electronic states are primarily contributed by the TMDs, which is the opposite of the MoS₂ and WS₂ systems. To illustrate this, Figures 2c and S1 show the band structure and CBM/VBM charge density distribution of a randomly selected heterostructure, 4,4-difluorocyclohexylammonium lead iodide ($[\text{F}_2\text{C}_6\text{H}_9\text{NH}_3]^2\text{PbI}_4/\text{MoTe}_2$).⁴⁶ The possible reason for this

difference is that monolayer MoS₂ and WS₂ have larger bandgaps (~ 1.5 eV) and typically exhibit n-type semiconductor behavior. The larger bandgaps may cause them to act as electron acceptors in the heterostructures, thus primarily contributing to the CB electronic states. In contrast, TMDs with smaller bandgaps (such as MoTe₂ and WTe₂, with bandgaps < 1.0 eV) may be more inclined to act as electron donors, primarily contributing to the VB electronic states. For other TMDs with bandgaps around ~ 1.2 eV, we observed mixed situations. In these heterostructures formed with 2D-LHPs, the electronic states of the CB and VB may be contributed by both the TMDs and 2D-LHPs, depending on the relative energy levels of the materials and the interface coupling strength. We calculated the differential charge density of $[\text{CH}_3(\text{CH}_2)_3\text{NH}_3]^2\text{PbI}_4/\text{MoS}_2$ and $[\text{F}_2\text{C}_6\text{H}_9\text{NH}_3]^2\text{PbI}_4/\text{MoTe}_2$ in Figure S2. The results show that charge redistribution primarily occurs at the heterojunction interface, manifested as electron loss on the organic layer side and electron accumulation on the TMDs side, demonstrating a significant interlayer charge transfer phenomenon in the heterostructure. This indicates that by selecting suitable TMDs and 2D-LHPs components, the electronic structure and charge transfer behavior of the heterostructures can be tuned to some extent. Furthermore, we noted that TMDs with smaller bandgaps tend to form type-I band alignments with 2D-LHPs, as shown in Figure 2b, and both the CB and VB are primarily contributed by the TMDs, as illustrated in Supplementary Figure S3. Although monolayer TMDs like MoSe₂ and MoTe₂ themselves have direct bandgaps, theoretically leading the type-I band alignment heterostructures to form direct bandgaps, our results show that type-I band alignments tend to form indirect bandgaps. This change in band dispersion relationship may be due to interface coupling and charge transfer, or strain effects caused by lattice mismatch. Given the significant application value of type-II heterostructures in the field of solar cells, we calculated the solar energy PCE of all type-II heterostructures using eq 1. During the calculation process, we excluded heterostructures with a bandgap less than 1 eV. This threshold was chosen to balance optimal light absorption, particularly in the visible spectrum, with minimizing thermal losses and maintaining high PCE in heterojunction structures. The calculation results are shown in Figure S4, where the highest heterostructure PCE reached an impressive 23.26%, while the majority of heterostructures had photoelectric conversion efficiencies concentrated around 19%. These results indicate that type-II heterostructures formed by TMDs and 2D-LHPs have immense application potential in the field of solar cells.

Recently, some reports have indicated that TMDs/2D-LHPs heterostructures can form S-type heterostructures, such as the WSe₂/BA₂PbI₄ heterostructure.¹⁴ Due to the S-scheme charge transfer mechanism, which helps achieve efficient charge separation and maximize redox capability, constructing S-type heterostructures holds great potential for applications in semiconductor photocatalytic technology. Here, we explore the potential of TMDs/2D-LHPs heterostructures in forming S-type heterostructures. According to the concept of two-dimensional S-type heterostructures proposed by Yu et al., an S-type heterostructure consists of a reduction photocatalyst (RP) and an oxidation photocatalyst (OP).^{47,48} The RP has a higher Fermi level (EF), lower CB and VB positions, and a lower work function compared to the OP, with its band alignment similar to a type-II heterostructure. Therefore, we

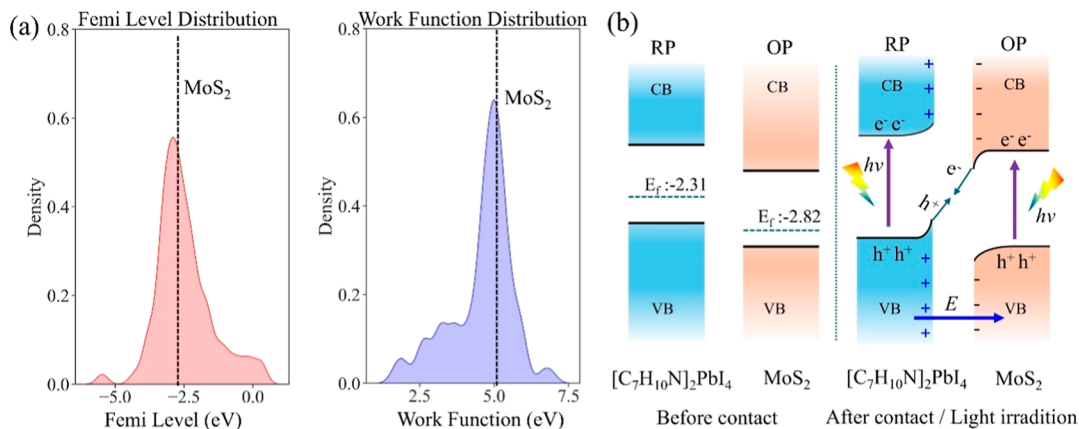


Figure 3. (a) Distribution of Fermi levels and work functions for 85 2D-LHPs, with the dashed line indicating the Fermi level and work function of MoS₂. (b) Energy band alignment diagrams of the PMA₂PbI₄/MoS₂ heterostructure before (left) and after (right) contact.

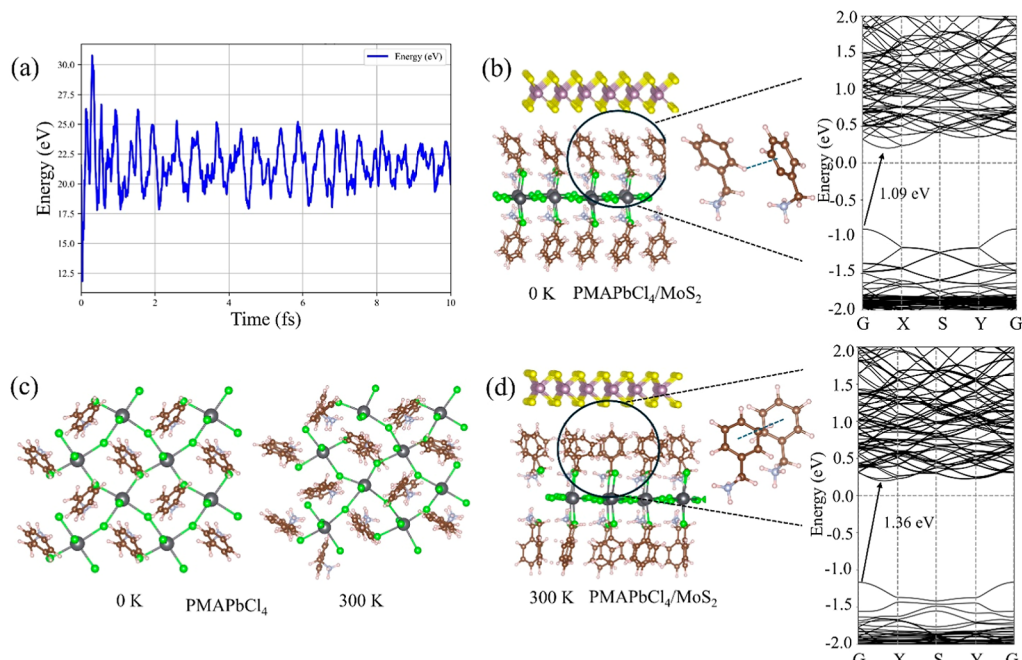


Figure 4. (a) Molecular dynamics simulation of the PMAPbCl₄/MoS₂ heterostructure at 300 K: time-energy relationship diagram. (b) Atomic configuration and corresponding band structure of the PMAPbCl₄/MoS₂ heterostructure at 0 K. (c) Comparison of molecular configurations of monolayer PMAPbCl₄ at 0 and 300 K. (d) Atomic configuration and corresponding band structure of the PMAPbCl₄/MoS₂ heterostructure at 300 K.

calculated the work functions and Fermi level distributions of 85 types of 2D-LHPs, with the results shown in Figure 3a. The calculated distributions of the Fermi levels and work functions of 2D-LHPs are quite broad, with Fermi levels mainly concentrated around $E_F = -3.0$ eV and work functions mainly around 5.0 eV. We also calculated the Fermi levels and work functions of monolayer TMDs and found that MoS₂ has a relatively lower Fermi level (-2.8 eV) and a higher work function (5.3 eV) compared to other TMDs, which is consistent with previous reports.⁴⁹ The specific calculation results for other TMDs can be found in Figure S5. Based on the statistical data, MoS₂/2D-LHPs are more likely to form type-II band alignment with lower CB and VB. Therefore, MoS₂ may have more potential as an OP. We have compiled the calculated S-type MoS₂/2D-LHPs heterostructures in the supplementary Table S1. In Figure 3b, we use the phenyl-methylammonium lead iodide (PMA₂PbI₄)/MoS₂ hetero-

structure as an example to describe how electrons transfer in this system, with PMA₂PbI₄ acting as the RP and molybdenum disulfide as the OP.⁵⁰ Before the contact between PMA₂PbI₄ and MoS₂, PMA₂PbI₄ has a higher Fermi level, while MoS₂ has a lower Fermi level. After the contact between PMA₂PbI₄ and OP, the electrons from the RP transfer to MoS₂ due to the difference in Fermi levels. At the interface, due to the loss of electrons, the Fermi level of PMA₂PbI₄ bends downward, and its band edges bend upward. At the same time, due to the gain of electrons, the Fermi level of MoS₂ bends upward, and its band edges bend downward. Consequently, PMA₂PbI₄ and OP reach equilibrium at their contact point. An internal electric field is formed at the interface, pointing from PMA₂PbI₄ to MoS₂. Under illumination, the internal electric field, band bending, and Coulomb force jointly induce photogenerated electrons to transfer from the CB of MoS₂ to the VB of PMA₂PbI₄. Ultimately, the photogenerated electrons in the CB

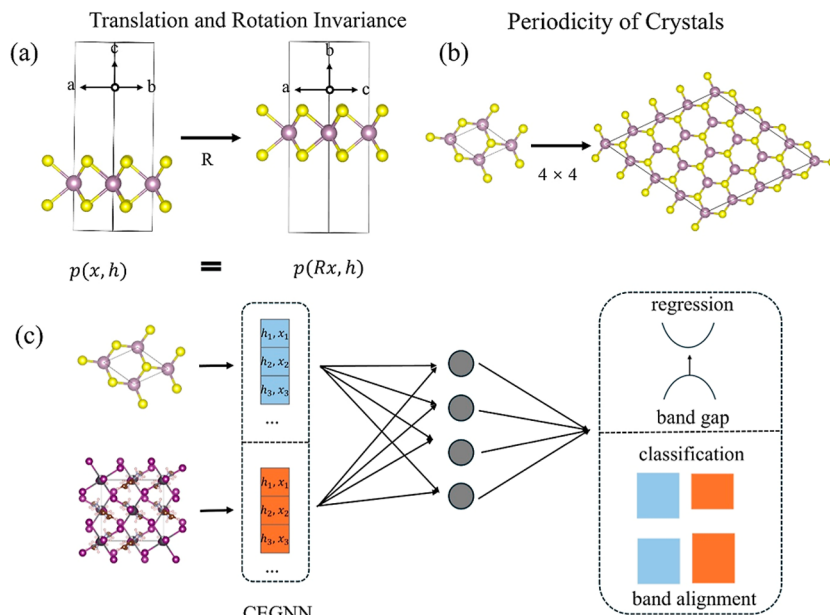


Figure 5. (a) Illustration of the translational and rotational invariance and periodicity of Crystals. (b) Shows that the physical properties of the crystal are consistent in both the unit cell and the supercell. (c) Illustrates the framework of the model, where experimental crystal structure coordinates are inputted to predict band gap size and band alignment type using CEGNN.

of PMA_2PbI_4 and the holes in the VB of MoS_2 are retained. These retained electrons and holes exhibit strong reduction and oxidation abilities, respectively. This result, similar to the performance of other heterostructure systems, demonstrates the immense potential of the $\text{PMA}_2\text{PbI}_4/\text{MoS}_2$ heterostructure in photocatalytic applications.^{51–53}

In 2D-LHPs, organic cation molecules may exhibit various molecular conformations due to the presence of rotatable chemical bonds. These differences in molecular conformations can significantly affect the electronic properties of materials, such as band structure and carrier mobility.^{54,55} Recent research has also confirmed that changes in the conformation of organic molecules have a significant impact on the electronic properties of perovskite materials.^{55–58} Therefore, we investigated whether the vdW interactions at the interface between TMDs and 2D-LHPs would affect the conformation of organic molecules. By screening the database, we selected the heterostructure formed by phenylmethylammonium lead chloride (PMAPbCl_4) and molybdenum disulfide (MoS_2) as the research object. The lattice mismatch of this heterostructure is less than 2%, allowing us to exclude the effects of strain. Additionally, experiments have shown that the conformation of organic molecules and the bandgap size of PMAPbCl_4 exhibit almost no significant changes within the temperature range of 0–400 °C.⁵⁹ Figure 4b shows the structure of the $\text{PMAPbCl}_4/\text{MoS}_2$ heterostructure, where the benzene rings in the PMA molecules are initially connected through C–H···π interactions. Based on DFT calculations, the bandgap of this heterostructure is 1.09 eV. We conducted molecular dynamics simulations at 300 K. Figure 4a shows that the $\text{PMAPbCl}_4/\text{MoS}_2$ heterostructure reached stability after running for 10 fs, with atomic motion stabilizing and energy fluctuations becoming minimal, indicating that the system is in a thermodynamic equilibrium state. Subsequently, we selected the conformation closest to the average structure for further analysis. The results indicate that π–π stacking interactions are formed between PMA molecules near the MoS_2 layer, and the

bandgap increases to 1.36 eV, as shown in Figure 4d. Further analysis reveals that the average Pb–Cl bond length decreases by 0.07 Å compared to the original structure. This may be due to the fact that the space occupied by the π–π stacking interactions is smaller than that of the C–H···π interactions, leading to lattice contraction and affecting the local electron cloud distribution and band structure. Meanwhile, we utilized molecular dynamics simulations to study the structural changes of monolayer PMAPbCl_4 at 300 K, as depicted in Figure 4c. It can be observed that, compared to the crystal structure at 0 K, no π–π stacking interactions are formed between PMA molecules in monolayer PMAPbCl_4 at 300 K, suggesting that the presence of MoS_2 may influence the conformational distribution of PMA molecules. Our results indicate that changes in the conformation of organic molecules in the organic layer have a significant impact on TMDs/2D-LHPs heterostructures, providing new insights for regulating the electronic properties of heterostructures. We also found that the chain length of the organic layer significantly affects the electronic structure of TMDs/2D-LHPs heterojunctions, as shown in Figure S6. Therefore, in the practical design of TMDs/2D-LHPs heterojunctions, the chain length of the organic layer can be used as a means to modulate their electronic properties.

Due to lattice mismatch, we only calculated the band structures of 602 heterostructures formed by 85 types of two-dimensional organic perovskites and TMDs. To predict the band structures of the remaining heterostructures formed by two-dimensional organic perovskites and TMDs, we hope to achieve this through machine learning methods. Traditional descriptor methods require complex descriptor calculations and screening, which are not suitable for large-scale screening. Moreover, the well-known crystal convolutional graph neural network (CGCNN) calculates two-dimensional graphs, ignoring the three-dimensional characteristics of molecules.³¹ Therefore, we intend to use the three-dimensional coordinates and atomic information on crystals as features to obtain the

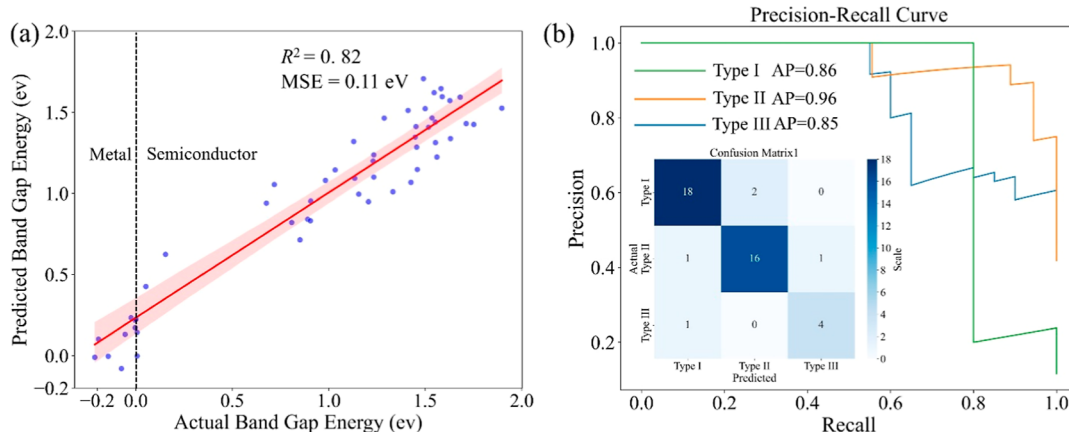


Figure 6. (a) Fitting results of the actual and predicted band gap values. (b) Confusion matrix and precision–recall curve for predicting band alignment types.

three-dimensional information on crystals and avoid using traditional descriptors. However, two-dimensional materials may face equivariance issues, as shown in Figure 5a. When the vacuum position or lattice direction of a 2D material changes, the atomic coordinates change accordingly, but its structure and electronic properties should remain unchanged. Thus, when using three-dimensional GNN, the model must ensure equivariance to molecular translation and rotation. Additionally, crystals have periodicity issues, where supercells of different sizes should have the same physical properties, as shown in Figure 5b. To address these issues, we designed the CEGNN model, which adopts the E(3) EGNN (EGNN). EGNN is a molecular representation method that can effectively capture the three-dimensional structural information on molecules. Using eqs 2–4, we constructed the EGNN model, as detailed in the Computational Method section. We also adopted CGCNN's method for handling periodicity. When constructing the graph, we consider not only atomic connections within the unit cell but also connections across periodic boundaries, as shown in eqs 5–10. This approach effectively represents the periodic structure of crystals, enabling the model to learn long-range interactions in crystals. The CEGNN model combines EGNN's equivariance and CGCNN's ability to handle periodicity, addressing both the equivariance issue of 2D materials and the periodicity issue of crystals. The specific algorithm will be detailed in the methods section. Considering the computational power and human resources required for constructing heterogeneous structures, we choose experimentally obtained crystal coordinates as input and feed the two materials into different EGNN networks separately, then concatenate the resulting vectors as input to a MLP (MLP) for regression and classification tasks, as shown in Figure 5c. In the regression task, we mainly predict the bandgap size of the heterogeneous structure; in the classification task, the main task is to distinguish the type of band alignment (type-I/II/III).

We initially randomly divided the entire data set into three subsets: 80% for training, 10% for validation, and 10% for testing. To evaluate the model's stability and generalization capability, we implemented a 10-fold cross-validation strategy on the training set. In this process, we randomly partitioned the training set into 10 equal-sized subsamples, each time retaining one subsample as validation data to test the model, while using the remaining 9 subsamples as training data. This

cross-validation process was repeated 10 times, ensuring that each subsample was used exactly once as validation data. We then averaged the results from all 10 folds to obtain a comprehensive assessment of the model's performance. For the regression task, we used the coefficient of determination (R^2) and mean squared error (MSE) to evaluate the results, as defined in eqs S1 and S2. For the classification task, we employed confusion matrices and precision–recall curves for evaluation, and provided detailed classification reports, with mathematical definitions given in eqs S3–S5. The cross-validation results showed that the model achieved an average R^2 of 0.8 and an average MSE of 0.11 eV, with specific data presented in Table S2. These results indicate that our model demonstrates good stability and predictive capability across different data subsets. For the independent test set, as shown in Figure 6, our model achieved an R^2 value of 0.82 and an MSE of 0.11 eV in the regression task. For the classification task, our model achieved an average precision of 0.86, 0.96, and 0.85 on the test set for predicting type-I, type-II, and type-III, respectively, indicating that the model can effectively distinguish between different types of band structures. The specific classification report can be found in Table S3. From the confusion matrix, it can be seen that the model performs well in classifying type-I and type-III, but there is some misclassification in type-III, which may be due to the relatively small number of type-III samples. Based on the predictions of our machine learning model, we systematically analyzed the band gaps and band alignments of all the heterostructures constructed from 2D-LHPs and TMDs. Among the 9,360 predicted heterostructures, approximately 83% exhibit semiconducting properties. The predicted band gap distribution is consistent with our results obtained using DFT calculations. For instance, the overall band gaps of MoS₂/2D-LHPs heterostructures are relatively small, while those of MoSe₂/2D-LHPs heterostructures are comparatively large. Regarding the band alignment types, about 33.6% of the heterostructures are classified as type-I, 37.5% as type-II, and 28.9% as type-III. Detailed prediction results have been uploaded to the github repository for reference.

CONCLUSION

This paper systematically investigates the band structure characteristics and influencing factors of heterostructures formed by transition metal TMDs and 2D-LHPs materials.

Through first-principles calculations, we constructed 602 types of TMDs/2D-LHPs heterostructures and analyzed their band alignment types. The results indicate that heterostructures formed by different TMDs and 2D perovskites exhibit different band alignment characteristics, which are closely related to the band gap sizes of the TMDs. TMDs with larger band gaps, such as MoS₂ and WS₂, are more likely to form type-II heterostructures with 2D perovskites, while TMDs with smaller band gaps, such as MoTe₂ and WTe₂, tend to form type-I heterostructures. Notably, MoS₂ can form ideal S-type heterostructures with specific 2D-LHPs, showing great potential in the field of photocatalysis. Additionally, we found that the interfacial interactions between TMDs and 2D-LHPs can significantly affect the conformation of organic molecules in the perovskite layer, leading to changes in the heterostructure band gaps. Based on the extensive band structure data of the heterostructures obtained, we constructed a CEGNN model to predict the electronic properties of heterostructures formed by TMDs and any 2D-LHPs. This study will provide important guidance for the rational design of novel high-performance TMDs/2D-LHPs heterostructure optoelectronic materials.

■ ASSOCIATED CONTENT

Data Availability Statement

To ensure real-time data updates and code optimization, all calculated data, predicted results, and utilized code will be available on GitHub: <https://github.com/xucongs/CEGNN>.

■ Supporting Information

The Supporting Information is available free of charge at <https://pubs.acs.org/doi/10.1021/acsami.4c11973>.

Additional methods and content ([PDF](#))

■ AUTHOR INFORMATION

Corresponding Author

Peiyuan Yu – Department of Chemistry and Shenzhen Grubbs Institute, Southern University of Science and Technology, 518055 Shenzhen, China;  orcid.org/0000-0002-4367-6866; Email: yup@ustech.edu.cn

Authors

Congsheng Xu – School of Chemistry and Chemical Engineering, Harbin Institute of Technology, 150001 Harbin, China; Department of Chemistry and Shenzhen Grubbs Institute, Southern University of Science and Technology, 518055 Shenzhen, China

Xiaomei Deng – Department of Chemistry and Shenzhen Grubbs Institute, Southern University of Science and Technology, 518055 Shenzhen, China

Complete contact information is available at:

<https://pubs.acs.org/doi/10.1021/acsami.4c11973>

Notes

The authors declare no competing financial interest.

■ ACKNOWLEDGMENTS

General: Computational work was supported by Center for Computational Science and Engineering at Southern University of Science and Technology and the CHEM high-performance supercomputer cluster (CHEM-HPC) located at department of chemistry, SUSTech. Funding: We are grateful

for the financial support from Southern University of Science and Technology (Y01216143).

■ REFERENCES

- (1) Lee, C.; Wei, X.; Kysar, J. W.; Hone, J. Measurement of the elastic properties and intrinsic strength of monolayer graphene. *science* **2008**, *321* (5887), 385–388.
- (2) Glavin, N. R.; Rao, R.; Varshney, V.; Bianco, E.; Apte, A.; Roy, A.; Ringe, E.; Ajayan, P. M. Emerging applications of elemental 2D materials. *Adv. Mater.* **2020**, *32* (7), 1904302.
- (3) Zhang, X.; Hou, L.; Ciesielski, A.; Samori, P. 2D materials beyond graphene for high-performance energy storage applications. *Adv. Energy Mater.* **2016**, *6* (23), 1600671.
- (4) Chhowalla, M.; Liu, Z.; Zhang, H. Two-dimensional transition metal dichalcogenide (TMD) nanosheets. *Chem. Soc. Rev.* **2015**, *44* (9), 2584–2586.
- (5) Bati, A. S.; Batmunkh, M.; Shapter, J. G. Emerging 2D layered materials for perovskite solar cells. *Adv. Energy Mater.* **2020**, *10* (13), 1902253.
- (6) Seyler, K. L.; Rivera, P.; Yu, H.; Wilson, N. P.; Ray, E. L.; Mandrus, D. G.; Yan, J.; Yao, W.; Xu, X. Signatures of moiré-trapped valley excitons in MoSe₂/WSe₂ heterobilayers. *Nature* **2019**, *567* (7746), 66–70.
- (7) Huang, X.; Zeng, Z.; Zhang, H. Metal dichalcogenide nanosheets: preparation, properties and applications. *Chem. Soc. Rev.* **2013**, *42* (5), 1934–1946.
- (8) Splendiani, A.; Sun, L.; Zhang, Y.; Li, T.; Kim, J.; Chim, C.-Y.; Galli, G.; Wang, F. Emerging photoluminescence in monolayer MoS₂. *Nano Lett.* **2010**, *10* (4), 1271–1275.
- (9) Guo, W.; Yang, Z.; Dang, J.; Wang, M. Progress and perspective in Dion-Jacobson phase 2D layered perovskite optoelectronic applications. *Nano Energy* **2021**, *86*, 106129.
- (10) Zhang, X.; Wu, G.; Yang, S.; Fu, W.; Zhang, Z.; Chen, C.; Liu, W.; Yan, J.; Yang, W.; Chen, H. Vertically oriented 2D layered perovskite solar cells with enhanced efficiency and good stability. *Small* **2017**, *13* (33), 1700611.
- (11) Fang, C.; Wang, H.; Shen, Z.; Shen, H.; Wang, S.; Ma, J.; Wang, J.; Luo, H.; Li, D. High-performance photodetectors based on lead-free 2D Ruddlesden–Popper perovskite/MoS₂ heterostructures. *ACS Appl. Mater. Interfaces* **2019**, *11* (8), 8419–8427.
- (12) Wang, Y.; Fullon, R.; Acerce, M.; Petoukhoff, C. E.; Yang, J.; Chen, C.; Du, S.; Lai, S. K.; Lau, S. P.; Voiry, D.; et al. Solution-processed MoS₂/organolead trihalide perovskite photodetectors. *Adv. Mater.* **2017**, *29* (4), 1603995.
- (13) Li, C.; Loh, K. P.; Leng, K. Organic-inorganic hybrid perovskites and their heterostructures. *Matter* **2022**, *5* (12), 4153–4169.
- (14) Xia, J.; Liang, C.; Gu, H.; Mei, S.; Cai, Y.; Xing, G. Two-dimensional heterostructure of MoS₂/BA₂PbI₄ 2D Ruddlesden–Popper perovskite with an S scheme alignment for solar cells: A first-principles study. *ACS Appl. Electron. Mater.* **2022**, *4* (4), 1939–1948.
- (15) Karpinska, M.; Liang, M.; Kempf, R.; Finzel, K.; Kamminga, M.; Dyksik, M.; Zhang, N.; Knodlseder, C.; Maude, D. K.; Baranowski, M.; et al. Nonradiative energy transfer and selective charge transfer in a WS₂/(PEA) 2PbI₄ heterostructure. *ACS Appl. Mater. Interfaces* **2021**, *13* (28), 33677–33684.
- (16) Wang, Q.; Zhang, Q.; Luo, X.; Wang, J.; Zhu, R.; Liang, Q.; Zhang, L.; Yong, J. Z.; Yu Wong, C. P.; Eda, G.; et al. Optoelectronic properties of a van der Waals WS₂ monolayer/2D perovskite vertical heterostructure. *ACS Appl. Mater. Interfaces* **2020**, *12* (40), 45235–45242.
- (17) Lai, H.; Lu, Z.; Lu, Y.; Yao, X.; Xu, X.; Chen, J.; Zhou, Y.; Liu, P.; Shi, T.; Wang, X.; et al. Fast, Multi-Bit, and Vis-Infrared Broadband Nonvolatile Optoelectronic Memory with MoS₂/2D-Perovskite Van der Waals Heterojunction. *Adv. Mater.* **2023**, *35* (6), 2208664.
- (18) Pan, D.; Fu, Y.; Spitha, N.; Zhao, Y.; Roy, C. R.; Morrow, D. J.; Kohler, D. D.; Wright, J. C.; Jin, S. Deterministic fabrication of

- arbitrary vertical heterostructures of two-dimensional Ruddlesden–Popper halide perovskites. *Nat. Nanotechnol.* **2021**, *16* (2), 159–165.
- (19) Panuganti, S.; Besteiro, L. V.; Vasileiadou, E. S.; Hoffman, J. M.; Govorov, A. O.; Gray, S. K.; Kanatzidis, M. G.; Schaller, R. D. Distance dependence of forster resonance energy transfer rates in 2D perovskite quantum wells via control of organic spacer length. *J. Am. Chem. Soc.* **2021**, *143* (11), 4244–4252.
- (20) Chen, Y.; Liu, Z.; Li, J.; Cheng, X.; Ma, J.; Wang, H.; Li, D. Robust interlayer coupling in two-dimensional perovskite/monolayer transition metal dichalcogenide heterostructures. *ACS Nano* **2020**, *14* (8), 10258–10264.
- (21) Zhang, Q.; Linardy, E.; Wang, X.; Eda, G. Excitonic energy transfer in heterostructures of quasi-2D perovskite and monolayer WS₂. *ACS Nano* **2020**, *14* (9), 11482–11489.
- (22) Xia, J.; Gu, H.; Liang, C.; Cai, Y.; Xing, G. Manipulation of Band Alignment in Two-Dimensional Vertical WSe₂/BA₂PbI₄ Ruddlesden–Popper Perovskite Heterojunctions via Defect Engineering. *J. Phys. Chem. Lett.* **2022**, *13* (20), 4579–4588.
- (23) Zhang, X.; Ding, B.; Wang, Y.; Liu, Y.; Zhang, G.; Zeng, L.; Yang, L.; Li, C. J.; Yang, G.; Nazeeruddin, M. K.; et al. Machine Learning for Screening Small Molecules as Passivation Materials for Enhanced Perovskite Solar Cells. *Adv. Funct. Mater.* **2024**, *34*, 2314529.
- (24) Lu, A. Y.; Martins, L. G. P.; Shen, P. C.; Chen, Z.; Park, J. H.; Xue, M.; Han, J.; Mao, N.; Chiu, M. H.; Palacios, T.; et al. Unraveling the Correlation between Raman and Photoluminescence in Monolayer MoS₂ through Machine-Learning Models. *Adv. Mater.* **2022**, *34* (34), 2202911.
- (25) Wei, J.; Chu, X.; Sun, X. Y.; Xu, K.; Deng, H. X.; Chen, J.; Wei, Z.; Lei, M. Machine learning in materials science. *InfoMat* **2019**, *1* (3), 338–358.
- (26) Yang, H.; Che, Y.; Cooper, A. I.; Chen, L.; Li, X. Machine Learning Accelerated Exploration of Ternary Organic Heterojunction Photocatalysts for Sacrificial Hydrogen Evolution. *J. Am. Chem. Soc.* **2023**, *145* (49), 27038–27044.
- (27) Liu, H.; Xu, L.; Ma, Z.; Li, Z.; Li, H.; Zhang, Y.; Zhang, B.; Wang, L.-L. Accurate prediction of semiconductor bandgaps based on machine learning and prediction of bandgaps for two-dimensional heterojunctions. *Mater. Today Commun.* **2023**, *36*, 106578.
- (28) Choudhary, K.; Garrity, K. F.; Hartman, S. T.; Pilania, G.; Tavazza, F. Efficient computational design of two-dimensional van der Waals heterostructures: Band alignment, lattice mismatch, and machine learning. *Phys. Rev. Mater.* **2023**, *7* (1), 014009.
- (29) Reiser, P.; Neubert, M.; Eberhard, A.; Torresi, L.; Zhou, C.; Shao, C.; Metni, H.; van Hoesel, C.; Schopmans, H.; Sommer, T.; et al. Graph neural networks for materials science and chemistry. *Commun. Mater.* **2022**, *3* (1), 93.
- (30) Fung, V.; Zhang, J.; Juarez, E.; Sumpter, B. G. Benchmarking graph neural networks for materials chemistry. *npj Comput. Mater.* **2021**, *7* (1), 84.
- (31) Xie, T.; Grossman, J. C. Crystal graph convolutional neural networks for an accurate and interpretable prediction of material properties. *Phys. Rev. Lett.* **2018**, *120* (14), 145301.
- (32) Park, C. W.; Wolverton, C. Developing an improved crystal graph convolutional neural network framework for accelerated materials discovery. *Phys. Rev. Mater.* **2020**, *4* (6), 063801.
- (33) Lin, X.; Jiang, H.; Wang, L.; Ren, Y.; Ma, W.; Zhan, S. 3D-structure-attention graph neural network for crystals and materials. *Mol. Phys.* **2022**, *120* (11), No. e2077258.
- (34) Zhang, B.; Zhou, M.; Wu, J.; Gao, F. Predicting the materials properties using a 3d graph neural network with invariant representation. *IEEE Access* **2022**, *10*, 62440–62449.
- (35) Satorras, V. G.; Hoogeboom, E.; Welling, M. E(n) equivariant graph neural networks. In *International conference on machine learning*; PMLR, 2021, pp 9323–9332.
- (36) Kaba, O.; Ravanbakhsh, S. Equivariant networks for crystal structures. *Adv. Neural. Inf. Process. Syst.* **2022**, *35*, 4150–4164.
- (37) Pakornchote, T.; Ektarawong, A.; Chotibut, T. StrainTensorNet: Predicting crystal structure elastic properties using SE (3)-equivariant graph neural networks. *Phys. Rev. Res.* **2023**, *5* (4), 043198.
- (38) Kresse, G.; Furthmüller, J. Efficient iterative schemes for ab initio total-energy calculations using a plane-wave basis set. *Phys. Rev. B* **1996**, *54* (16), 11169–11186.
- (39) Perdew, J. P.; Burke, K.; Ernzerhof, M. Generalized Gradient Approximation Made Simple. *Phys. Rev. Lett.* **1996**, *77* (18), 3865–3868.
- (40) Grimme, S.; Antony, J.; Ehrlich, S.; Krieg, H. A consistent and accurate ab initio parametrization of density functional dispersion correction (DFT-D) for the 94 elements H–Pu. *J. Chem. Phys.* **2010**, *132* (15), 154104.
- (41) Kühne, T. D.; Iannuzzi, M.; Del Ben, M.; Rybkin, V. V.; Seewald, P.; Stein, F.; Laino, T.; Khalil, R. Z.; Schütt, O.; Schiffmann, F.; et al. CP2K: An electronic structure and molecular dynamics software package-Quickstep: Efficient and accurate electronic structure calculations. *J. Chem. Phys.* **2020**, *152* (19), 194103.
- (42) Goedecker, S.; Teter, M.; Hutter, J. Separable dual-space Gaussian pseudopotentials. *Phys. Rev. B* **1996**, *54* (3), 1703–1710.
- (43) Scharber, M. C.; Mühlbacher, D.; Koppe, M. Design rules for donors in bulk-heterostructure solar cells-Towards 10% energy-conversion efficiency. *Adv. Mater.* **2006**, *18* (6), 789–794.
- (44) Marchenko, E. I.; Fateev, S. A.; Petrov, A. A.; Korolev, V. V.; Mitrofanov, A.; Petrov, A. V.; Goodlin, E. A.; Tarasov, A. B. Database of two-dimensional hybrid perovskite materials: open-access collection of crystal structures, band gaps, and atomic partial charges predicted by machine learning. *Chem. Mater.* **2020**, *32* (17), 7383–7388.
- (45) Menahem, M.; Dai, Z.; Aharon, S.; Sharma, R.; Asher, M.; Diskin-Posner, Y.; Korobko, R.; Rappe, A. M.; Yaffe, O. Strongly anharmonic octahedral tilting in two-dimensional hybrid halide perovskites. *ACS Nano* **2021**, *15* (6), 10153–10162.
- (46) Sha, T. T.; Xiong, Y. A.; Pan, Q.; Chen, X. G.; Song, X. J.; Yao, J.; Miao, S. R.; Jing, Z. Y.; Feng, Z. J.; You, Y. M.; et al. Fluorinated 2D lead iodide perovskite ferroelectrics. *Adv. Mater.* **2019**, *31* (30), 1901843.
- (47) Yuan, Y.; Guo, R.-t.; Hong, L.-f.; Ji, X.-y.; Lin, Z.-d.; Li, Z.-s.; Pan, W.-g. A review of metal oxide-based Z-scheme heterojunction photocatalysts: actualities and developments. *Mater. Today Energy* **2021**, *21*, 100829.
- (48) Zhu, B.; Sun, J.; Zhao, Y.; Zhang, L.; Yu, J. Construction of 2D S-Scheme Heterojunction Photocatalyst. *Adv. Mater.* **2024**, *36* (8), 2310600.
- (49) Kim, H.-g.; Choi, H. J. Thickness dependence of work function, ionization energy, and electron affinity of Mo and W dichalcogenides from DFT and GW calculations. *Phys. Rev. B* **2021**, *103* (8), 085404.
- (50) Schmitt, T.; Bourelle, S.; Tye, N.; Soavi, G.; Bond, A. D.; Feldmann, S.; Traore, B.; Katan, C.; Even, J.; Dutton, S. E.; et al. Control of crystal symmetry breaking with halogen-substituted benzylammonium in layered hybrid metal-halide perovskites. *J. Am. Chem. Soc.* **2020**, *142* (11), 5060–5067.
- (51) Zhu, H.; Zhang, X.; Nie, Y.; Yang, D.; Xiang, G. 2D/2D Janus BiTeCl/GeSe vdW heterostructure as a robust high-performance S-scheme photocatalyst for water splitting. *Appl. Surf. Sci.* **2023**, *635*, 157694.
- (52) Bao, J.; Zhu, B.; Zhang, F.; Chen, X.; Guo, H.; Qiu, J.; Liu, X.; Yu, J. Sc2CF2/Janus MoS₂ heterostructure: a potential Z-scheme photocatalyst with ultra-high solar-to-hydrogen efficiency. *Int. J. Hydrogen Energy* **2021**, *46* (80), 39830–39843.
- (53) Li, C.; Liang, H.; Xu, Z.; Tao, J.; Zhang, Y.; Dong, K.; Wang, L.-L.; Xu, L. Construction of Z-scheme InN/BTe heterostructure for enhanced photocatalytic hydrogen evolution: DFT calculation and mechanism study. *Int. J. Hydrogen Energy* **2024**, *68*, 289–296.
- (54) Ghorabe, F. D.; Novikov, A. S.; Nesterov, P. V.; Galina, A. R.; Dudaev, A. E.; Shishatskaya, E. I.; Skorb, E. V. Insight on relationship between crystallinity and band gap energies of polyhydroxyalkanoates polymers. *Mater. Today Commun.* **2024**, *39*, 108886.

(55) Friederich, P.; Meded, V.; Poschlade, A.; Neumann, T.; Rodin, V.; Stehr, V.; Symalla, F.; Danilov, D.; Lüdemann, G.; Fink, R. F.; et al. Molecular origin of the charge carrier mobility in small molecule organic semiconductors. *Adv. Funct. Mater.* **2016**, *26* (31), 5757–5763.

(56) Dong, K.; Yang, X.; Yao, F.; Cong, H.; Zhou, H.; Zhou, S.; Cui, H.; Wang, S.; Tao, C.; Sun, C.; et al. Spacer Conformation Induced Multiple Hydrogen Bonds in 2D Perovskite toward Highly Efficient Optoelectronic Devices. *Adv. Mater.* **2024**, *36*, 2313889.

(57) Chang, J.-K.; Sadhukhan, P.; Myoung, J.-M. High-performance pure red perovskite light-emitting diodes utilizing conformational transformation of ionic liquid additive. *Nano Energy* **2024**, *120*, 109228.

(58) Li, C.; Yang, J.; Su, F.; Tan, J.; Luo, Y.; Ye, S. Conformational disorder of organic cations tunes the charge carrier mobility in two-dimensional organic-inorganic perovskites. *Nat. Commun.* **2020**, *11* (1), 5481.

(59) Liao, W.-Q.; Zhang, Y.; Hu, C.-L.; Mao, J.-G.; Ye, H.-Y.; Li, P.-F.; Huang, S. D.; Xiong, R.-G. A lead-halide perovskite molecular ferroelectric semiconductor. *Nat. Commun.* **2015**, *6* (1), 7338.